

**How Ice Bridges the Gap**

Journal:	<i>Soft Matter</i>
Manuscript ID	SM-ART-10-2019-001968.R1
Article Type:	Paper
Date Submitted by the Author:	07-Nov-2019
Complete List of Authors:	Nath, Saurabh; Virginia Polytechnic Institute and State University, Biomedical Engineering and Mechanics Ahmadi, S.; Virginia Polytechnic Institute and State University, Biomedical Engineering and Mechanics Boreyko, Jonathan; Virginia Polytechnic Institute and State University, Mechanical Engineering

Cite this: DOI: 00.0000/xxxxxxxxxx

Received Date

Accepted Date

DOI: 00.0000/xxxxxxxxxx

## How Ice Bridges the Gap<sup>†</sup>

Saurabh Nath,<sup>a,b</sup> S. Farzad Ahmadi,<sup>a,c</sup> and Jonathan B. Boreyko<sup>a,c</sup>

When supercooled dew droplets form on a chilled surface, the subsequent freezing process is driven by a fascinating phenomenon of propagating inter-droplet ice bridges. Here, we explore the range of conditions under which an individual ice dendrite can successfully bridge the gap from a frozen droplet to its nearest liquid neighbor. Ranging the droplet sizes from  $1\ \mu\text{m}$ – $10\ \text{mm}$ , we find that the criterion for ice bridging is purely geometric and independent of temperature, ambient humidity, and surface wettability. We model the growth of individual ice bridges as well as the global speed of percolating fronts sweeping across large droplet populations. We also give a dynamical law for dry zone formation when ice fails to bridge the gap.

In 1911 Alfred Wegener, the father of continental drift, realized the importance of the hygroscopic nature of ice in the context of mixed-phase cloud behavior. He hypothesized that the depressed vapor concentration of ice particles compared to supercooled water droplets is responsible for the glaciation of mixed-phase clouds: ice droplets grow while the supercooled liquid droplets evaporate.<sup>1–3</sup> While atmospheric scientists have been modeling the importance of hygroscopic ice for a century,<sup>4</sup> it has only been in the past decade that surface scientists equally appreciated its importance for the process of condensation frosting on chilled substrates.

In 2010, J. B. Dooley made the first observation that when a population of supercooled dew droplets on a surface freezes, it occurs via a propagation of inter-droplet ice bridges. These bridges grow from frozen droplets to their nearest neighboring liquid droplets, spreading ice like a ‘wildfire’ across the plane of the surface.<sup>5</sup> As with glaciation in clouds, the proposed mechanism for these beautiful ‘wildfires’ is the depressed saturation vapor concentration of with respect to liquid water at the same subfreezing temperature.<sup>5–8</sup>

Inter-droplet ice bridging during nascent stages of condensation frosting has subsequently been experimentally visualized by multiple groups independently.<sup>6,7,9</sup> The proposed mechanism goes as follows - a frozen droplet serves as a humidity sink to its liquid neighbors, causing these droplets to evaporate even when the ambient vapor is highly supersaturated.<sup>5–7</sup> Vapor emanating from a liquid droplet diffuses toward an adjacent ice droplet and deposits as a growing ice bridge. The liquid droplet freezes as

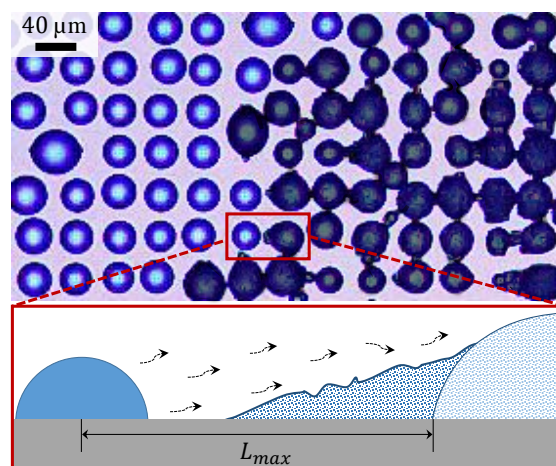


**Fig. 1** Frost percolating across a supercooled condensate population at  $T_w = -10\ ^\circ\text{C}$ ,  $T_\infty = 24.0\ ^\circ\text{C}$ , and humidity  $RH = 26\%$ . The frozen droplets and ice bridges have been false-colored black. Inset: Schematic of diffusive vapor exchange between a pair of droplets, one liquid and one frozen, leading to the formation of a directed ice bridge.

soon as the ice bridge connects, triggering the next iteration of bridging towards another liquid droplet.<sup>5–7,10–12</sup>

However, if the gap between two droplets is sufficiently large, the liquid droplet can completely evaporate before the bridge can connect.<sup>5–7</sup> In this article, we first identify the connection criterion for an ice bridge in a pairwise interaction where the droplet size is ranged from micro-droplets to puddles. Second, we develop a model that captures both the local speed of a growing ice bridge and the global speed of the percolation front.

An experimental demonstration of inter-droplet ice bridging across a population of dropwise condensate is shown in Fig.1. Droplets preferentially nucleated on an array of  $10\ \mu\text{m}$  hydrophilic circles patterned onto a hydrophobic silicon wafer, with the fabrication details provided in a previous report.<sup>13</sup> During condensation frosting, frozen droplets are all connected via ice

<sup>a</sup> Department of Biomedical Engineering and Mechanics, Virginia Tech, Blacksburg, VA 24061, U.S.A.

<sup>b</sup> Physique et Mécanique des Milieux Hétérogènes, UMR 7636 du CNRS, ESPCI – 75005, Paris, France, EU.

<sup>c</sup> Department of Mechanical Engineering, Virginia Tech, Blacksburg, VA 24061, U.S.A.

<sup>†</sup> Electronic Supplementary Information (ESI) available. See DOI: 10.1039/cXsm00000x/

bridges even though the liquid droplets are not yet large enough to touch each other. To fully characterize the ice bridging, we systematically vary the interdroplet distance, the diameters of the liquid droplet ( $D_l$ ) and the frozen droplet ( $D_i$ ), the substrate temperature ( $T_w$ ), the ambient humidity ( $RH$ ), and the surface wettability.

The behavior of the ice bridges varied depending on the sizes of the droplets relative to each other,  $\kappa = D_l/D_i$ , and to the capillary length,  $l_c \sim 1$  mm for water. Droplets smaller than  $l_c$  are spherically capped, whereas gravity dominates above  $l_c$  to form flattened puddles. Fig. 2A shows a regime map of the four different types of ice bridging behavior we observed broken down by the droplet geometry: (I) liquid droplet and larger frozen droplet or puddle ( $D_l < l_c$ ,  $\kappa < 1$  or  $\kappa \ll 1$ ), (II) liquid droplet and smaller frozen droplet ( $D_l < l_c$ ,  $\kappa > 1$ ), (III) liquid puddle and frozen droplet ( $D_l > l_c$ ,  $\kappa \gg 1$ ), and (IV) liquid puddle and frozen puddle ( $D_l > l_c$ ,  $D_i > l_c$ ).

For Regimes I and II, experiments were conducted on the aforementioned chemical micropatterns. Near one edge of each hydrophilic array there was a large hydrophilic rectangle (4 mm  $\times$  8 mm). Each experimental trial involved depositing 10  $\mu$ L of wa-

ter on this rectangle and cooling the substrate to  $T_w = -10^\circ\text{C}$  to grow microscopic condensation on the hydrophilic circle array. At some desired time, a small ice cube was touched to the water film on the rectangle to freeze the puddle. This would commence the percolation of inter-droplet ice bridges, initially from the frozen puddle to the first row of condensate (Regime I) and subsequently across the population of condensate (I and II). For interactions involving liquid puddles, either one (Regime III) or two (IV) millimetric liquid droplets were deposited on a smooth and uniformly hydrophobic silicon substrate ( $\theta_f = 89^\circ \pm 1^\circ$  and  $\theta_a = 113^\circ \pm 1^\circ$ ). The surface was then chilled in the same manner as the micropatterned surface to initiate condensation frosting. In all cases, ambient conditions were  $T_\infty = 24.0 \pm 0.9^\circ\text{C}$  and  $RH = 26 \pm 2\%$ .

It has been previously observed that if the initial distance between the ice and the first row of condensate droplets is sufficiently large, the ice bridges will fail to connect. Instead, the condensate droplets will completely evaporate row by row until reaching a dry zone of stable width  $\delta_{Cr}$ .<sup>7,13–17</sup> Here, we bring attention to the growing ice front, which initially exhibits a uniform profile. However, when the condensation is sufficiently far away from the ice front, this desublimation front eventually destabilizes in a manner reminiscent of the Mullins–Sekerka instability (Fig. 2B), with a constant wavelength of  $\lambda \sim \theta(10\ \mu\text{m})$ .<sup>18</sup> Furthermore, bridges growing to lengths of 100  $\mu\text{m}$  or larger exhibited side-branching and tip-splitting deformities (Fig. 2C). In this report, we focus on short bridge lengths,  $L_b \lesssim \lambda$ , where the instability was suppressed to instigate the preferential growth of a unidirectional ice bridge with little or no side-branches along its length. (Fig. 2D). Here,  $L_b$  is the length of an ice bridge, measured from the edge of the frozen droplet to its final extent where it either touches a liquid droplet or causes the droplet to completely evaporate.

*Criterion for Connection:* For a given pair of droplets, the maximum extent to which an ice bridge can grow is geometrically constrained by the distance  $L_{max}$  from the edge of the frozen droplet to the center of the liquid droplet (Fig. 1). We can define a dimensionless separation parameter,  $S^* = L_{max}/D_l$ , where ice bridging fails above a critical value:  $S^* > S_{Cr}^*$ . The value of  $S_{Cr}^*$  can be extracted from conservation of mass, as the mass of a complete ice bridge cannot exceed that of the liquid droplet feeding the bridge ( $M_l \sim M_b$ ). It was previously argued that  $S_{Cr}^* \sim 1$ ;<sup>6</sup> here, we reveal that the value of  $S_{Cr}^*$  varies between the four regimes.

For Regimes I and II, the mass of the spherical-cap liquid droplet scales as  $M_l \sim \rho D_l^3$ . Top-down microscopy revealed that when  $\kappa < 1$ , the width of the ice bridge extending from the frozen droplet scaled as the diameter of the adjacent liquid droplet  $D_l$ . We hypothesize that the ice bridge height also scales as  $D_l$ , as the liquid droplet is diffusively growing the bridge (Fig. 3A). This leads to  $M_b \sim \rho D_l^2 L_b$  for  $\kappa < 1$ . When  $\kappa > 1$ , the base of the bridge is now constrained by the area  $D_i^2$  (Fig. 3B). Thus,  $M_b \sim \rho D_i^2 L_b$ . Setting  $M_l \sim M_b$ , we obtain the contrasting ice bridging criteria for Regimes I and II, respectively:

$$S^* \leq S_{Cr}^* \sim \begin{cases} 1, & \text{if } \kappa < 1. \\ \kappa^2, & \text{if } \kappa > 1. \end{cases} \quad (1)$$

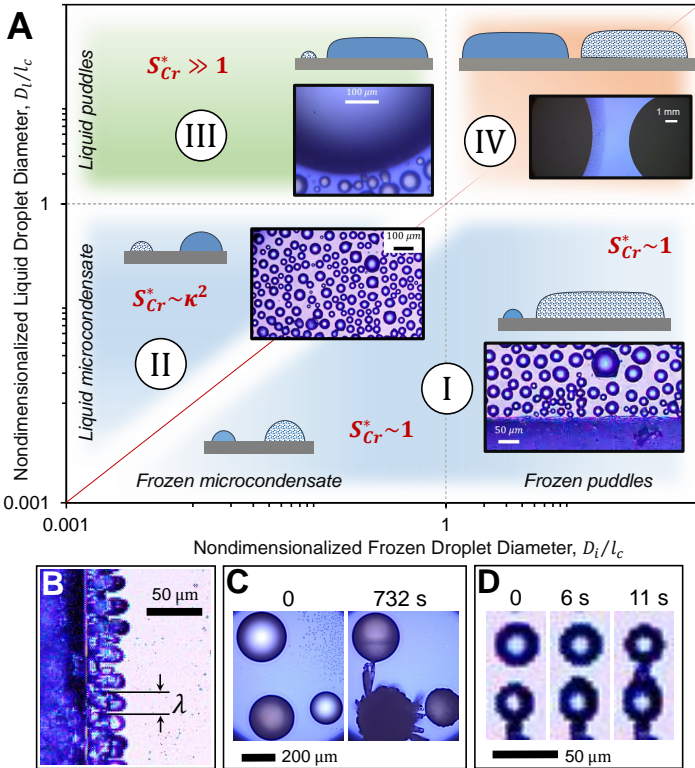


**Fig. 2** (A) Regime map of the different geometric modes of inter-droplet ice bridging. Insets show schematics and micrographs for each regime. The red line divides the phase space into two regions:  $\kappa > 1$  (above) and  $\kappa < 1$  (below), where  $\kappa = D_l/D_i$ . The blue region corresponds to the regimes where bridges could either succeed or fail (Regimes I and II), in the green region bridging was always successful (III), and no bridging was observed in the orange region (IV). (B) In the absence of any liquid microcondensate sufficiently close to the frozen droplet, its planar ice front destabilizes with a wavelength  $\lambda$ . (C) Successful ice bridges of length  $L_b/\lambda \gg 1$  exhibited tip-splitting (bridge on the right) and step morphology (upper bridge). (D) Successful ice bridging for  $L_b/\lambda \lesssim 1$ .

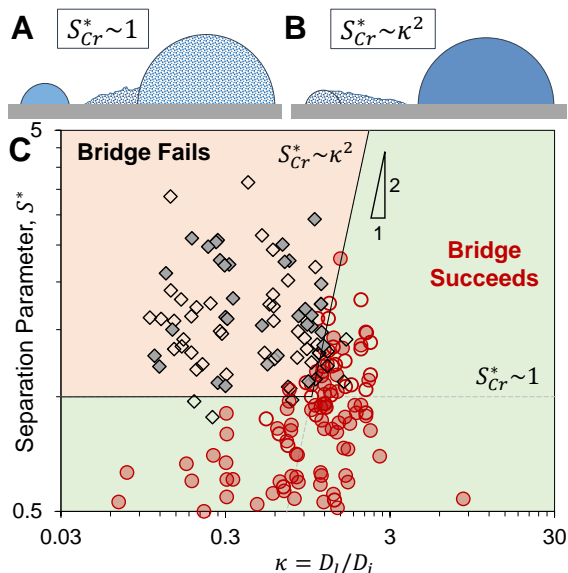


**Fig. 3** (A) When the frozen droplet is larger, the cross-sectional area of the ice bridge is constrained by the size of the liquid droplet facilitating its growth. (B) When the liquid droplet is larger, the ice bridge is instead constrained by the frozen droplet it is extending from. (C) Phase map of the success and failure of ice bridges for Regimes I and II. The red circles denote successfully completed ice bridges, while gray diamonds represent bridge failure. Data points correspond to experiments on the uniform hydrophobic and chemically micropatterned surfaces, at  $-10^\circ\text{C}$  and  $-20^\circ\text{C}$ . Filled data points represent isolated pairwise interactions, while the open symbols represent multi-droplet interactions (see Fig. S2 in the Supplemental Material). Solid lines correspond to Eq. 1 with a pre-factor of 1.

Fig. 3C shows a phase map where the experimentally measured  $S^*$  values are plotted against their corresponding  $\kappa$  values. A clear demarcation between failed and completed ice bridges is seen at  $S_{Cr}^* \sim 1$  when the liquid droplet is smaller and at  $S_{Cr}^* \sim \kappa^2$  when the frozen droplet is smaller, just as predicted by Eq. 1.

Ice bridging from a frozen droplet to a liquid puddle (Regime III) was found to be always successful. The mass of a liquid puddle scales as  $M_l \sim \rho D_l^2 l_c$ , while  $M_b \sim \rho D_l^2 L_b$ . Therefore,  $S_{Cr}^* \sim \kappa^2 l_c/D_l \gg 1$ , as  $D_l > 10D_i$ . The diameter of the liquid puddle is always larger than the typical inter-droplet distance of  $100\ \mu\text{m}$ , such that  $S^* < 1$  for Regime III. It follows that  $S^* < S_{Cr}^*$ , such that ice bridges are always successful (Fig. S1).

In contrast, for Regime IV (two puddles), whichever puddle froze first was never able to successfully freeze the other puddle via ice bridging. An annular ring of liquid micro-condensate was observed to form about each liquid puddle, which would not evaporate even after setting the humidity of the chamber to nearly zero (see inset of Fig 2A, Regime IV). This suppression of evaporation can be attributed to the local supersaturation engendered by a vapor-rich dome that forms between large droplets/puddles placed next to each other.<sup>19</sup> Once one of the two deposited puddles froze, it started interacting with the intermediate micro-condensate rather than the other puddle (i.e. Regimes I and/or III).

**Bridge Growth Rate:** In this section we are interested in finding out the average bridge growth rate between two droplets in a monodisperse population of condensate ( $\kappa \approx 1$ ). In a pairwise in-

teraction, the velocity of a growing ice bridge was observed to be constant, as long as it is unbranched and unchanged in curvature. This is seen in Fig. 4A, where we have plotted the final bridge lengths,  $L_b$  against total time of growth,  $\tau$ , from extensive condensation frosting experiments on hydrophobic surfaces at  $-10^\circ\text{C}$  and  $-20^\circ\text{C}$ . We see that at a given temperature, the growth rate is constant irrespective of the size and success/failure of the bridge:  $v_b \approx 1.3\ \mu\text{m/s}$  for  $-10^\circ\text{C}$  and  $v_b \approx 1.7\ \mu\text{m/s}$  for  $-20^\circ\text{C}$ . Fig. 4B corresponds to experiments done on superhydrophobic surfaces ( $\theta \approx 160^\circ$ ) at  $-10^\circ\text{C}$  and  $-20^\circ\text{C}$ , where the velocities come out to be  $v_b \approx 0.8\ \mu\text{m/s}$  and  $1.8\ \mu\text{m/s}$  respectively. The constancy of these values reveal that the ice bridging growth rates seem insensitive to substrate wettability.

Invoking an electrostatic analogy where the ice bridge is the analogous electrical conductor,  $m_b = \int_A \mathcal{D} \vec{\nabla} c \cdot \hat{n} dA = 4\pi \mathcal{D} C \Delta c$ , where  $\mathcal{D}$  is the diffusivity of water vapor in air,  $C$  is the ‘‘capaci-

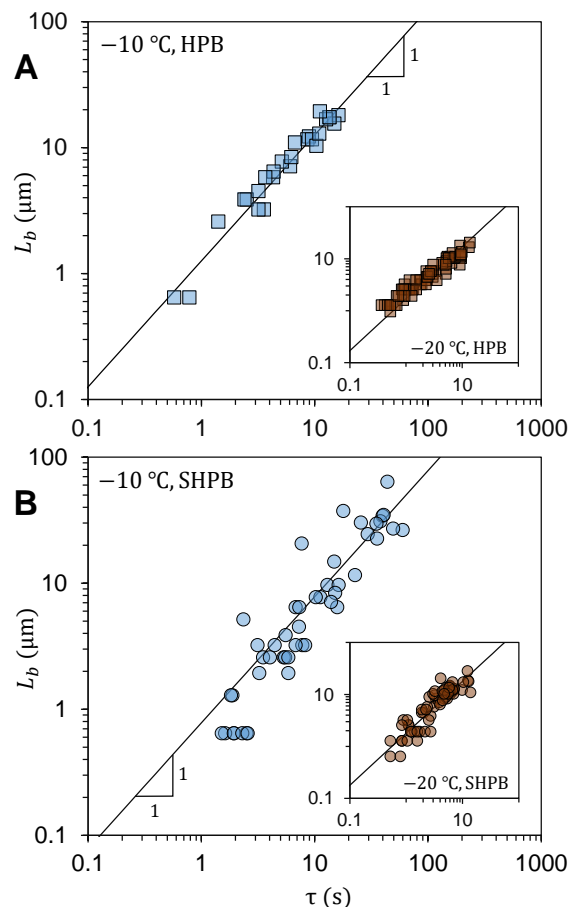


**Fig. 4** Final lengths of ice bridges ( $L_b$ ), for both successful or failed connections, plotted against their total time of growth. (A) and (B) correspond to experiments on hydrophobic (HPB) and superhydrophobic surfaces (SHPB) respectively. Solid lines represent best fits to Eq. 2. Experiments were conducted with ambient conditions of  $T_\infty = 22 \pm 1$  and  $RH = 45 \pm 3\%$ . The substrate was thermally bonded to a Peltier stage and chilled to either  $-10^\circ\text{C}$  (primary graphs) or  $-20^\circ\text{C}$  (insets). The high degree of supersaturation engendered supercooled condensation; after about 100 s ice nucleation occurred in a small subset of droplets (typically at the edges of substrate), triggering in-plane frost growth across the population of condensate as a percolating network of ice bridges.

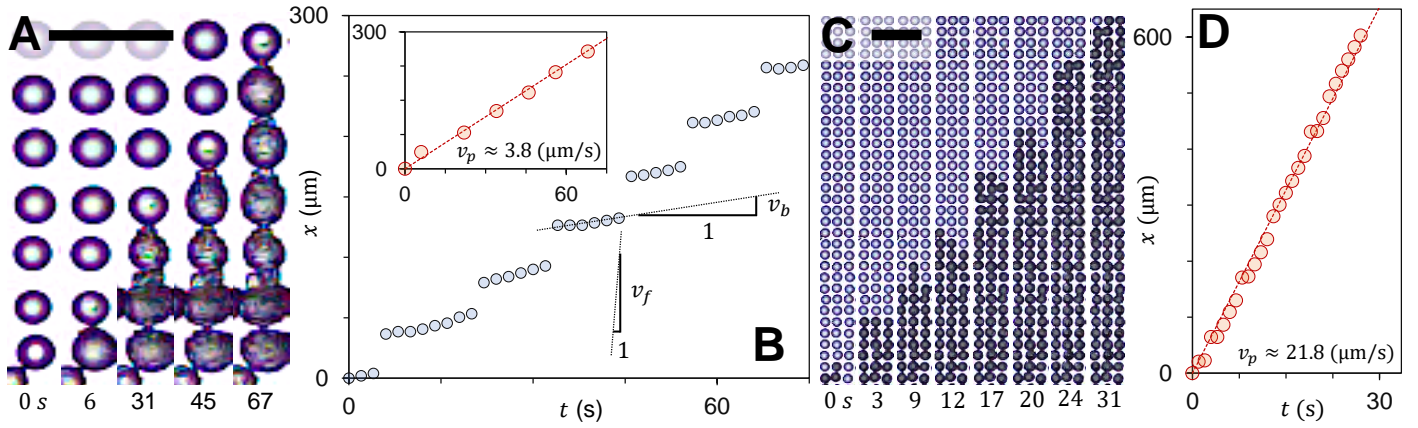


**Fig. 5** (A) Time-lapse sequence of 1D percolation: Successive freezing of six  $30\ \mu\text{m}$  droplets, with average separation  $\langle S^* \rangle = 1.06$ , by formation of ice bridges at  $T_w = -10^\circ\text{C}$ ,  $T_\infty = 24^\circ\text{C}$ , and  $RH = 26\%$ . The scale bar represents  $100\ \mu\text{m}$ . (B)  $x-t$  plot of the freezing front reveals step-like behavior, due to inter-droplet freezing being much slower than intra-droplet freezing ( $v_b \ll v_f$ ). Inset: Same plot with only the first point of each step. Dotted line corresponds to a coarse-grained percolation speed,  $v_p \approx 3.8\ \mu\text{m/s}$ . (C) Percolation through a denser packing with  $\langle S^* \rangle = 0.61$ . The frozen droplets are false-colored black (see Fig. S3 in the Supplemental Material for original figure). The scale bar represents  $100\ \mu\text{m}$ . (D) The resulting  $x-t$  plot shows that there is a constant percolation velocity of  $v_p \approx 21.8\ \mu\text{m/s}$ .

tance,” and  $\Delta c = (c_1 - c_i)$  is the temperature-dependent difference in saturated vapor concentration.<sup>20</sup> In general, one can write  $\mathbb{C} = \beta D_i$ , where  $\beta$  is a geometric parameter that depends on the morphology of the growing crystal.<sup>21</sup> Assuming an unbranched growth from a hemispherical frozen droplet and monodisperse droplets ( $\kappa \approx 1$ ),  $\dot{m}_b \approx \rho v_b \pi D_i^2 / 8$  for any bridge. Therefore the average bridge growth rate in a population is

$$\langle v_b \rangle \approx \beta \frac{\mathcal{D} \Delta c}{\rho} \frac{32}{\langle D_i \rangle}, \quad (2)$$

where  $\langle D_i \rangle$  is the mean droplet diameter in the population.

The geometric parameter  $\beta$  of Eq. 2 can be captured if we plug in the experimentally measured growth rate  $\langle v_b \rangle$  and mean droplet diameter of the population. This revealed  $\beta$  values of 0.32 at  $-10^\circ\text{C}$  and 0.39 at  $-20^\circ\text{C}$  for hydrophobic surfaces and 0.14 at  $-10^\circ\text{C}$  and 0.33 at  $-20^\circ\text{C}$  for superhydrophobic surfaces. We note that for our experiments on the  $-10^\circ\text{C}$  superhydrophobic surface, the mean diameter of the freezing droplets is  $\langle D_i \rangle = 30 \pm 20\ \mu\text{m}$  at  $-10^\circ$ , where clearly the monodispersity assumption breaks down. However the theoretical assumption of monodisperse droplets reasonably holds for our experiments on hydrophobic surfaces where the standard deviations in size of the freezing droplets were only  $\langle D_i \rangle = 49 \pm 9\ \mu\text{m}$  and  $26 \pm 7\ \mu\text{m}$  at  $-10^\circ\text{C}$  and  $-20^\circ\text{C}$  and for superhydrophobic surfaces at  $-20^\circ\text{C}$  where  $\langle D_i \rangle = 26 \pm 9\ \mu\text{m}$  for  $-20^\circ\text{C}$ .

These observations reveal an averaged value of  $\beta \approx 0.35$  for monodisperse droplet populations that does not vary with surface wettability or temperature. It is beyond the scope of this paper to analyze why the value is 0.35. However, unlike regular surfaces, superhydrophobic surfaces can exhibit larger variations in average bridge growth rates as droplet populations on these surfaces are typically polydisperse because of the jumping-droplet phenomenon.<sup>22</sup> A second factor that might contribute to dispersing the data is that the surface roughness of a superhydrophobic surface can add a three-dimensional tortuosity to the propagating ice bridges.<sup>10</sup>

The above description makes an implicit assumption that the line friction on an ice crystal growing along a solid substrate is negligible. While a theoretical reasoning for this assumption is lacking, experimentally it can be backed up by the observations of Petit et al.,<sup>23</sup> where they find that growth rate of ice bridges are independent of the viscoelastic properties of the solid.

*Global Frost Percolation:* Now that we have given a local description of pairwise interactions in condensation frosting, herein we will describe the global dynamics of condensation frosting for the two limiting cases of all bridges connecting ( $S^* < S_{Cr}^*$ ) or all bridges failing ( $S^* > S_{Cr}^*$ ). Although a typical inter-droplet frost front has local regions of both success and failure,<sup>5-7</sup> usually one of these modes is the dominant one such that the global behavior can be approximated by these limiting cases.

*$S^* < S_{Cr}^*$  everywhere:* In a dense monodisperse population of  $10\ \mu\text{m}$  droplets separated by distances of the order of  $1\ \mu\text{m}$ , the percolation front velocities are  $v_p \sim 10\ \mu\text{m/s}$ , about ten times greater than the characteristic bridge growth rate.<sup>13</sup> This can be rationalized by realizing a percolating frost front involves both the propagation of ice bridges (desublimation) and the freezing of liquid droplets, the latter being a significantly faster process. The intra-droplet freezing velocity,  $v_f$ , can be estimated by balancing the droplet’s latent heat of fusion with its conduction of heat into the substrate,  $\rho v_f h_{sl} \sim k_i \Delta T / D_i$ . The latent heat of freezing for water scales as  $h_{sl} \sim 10^5\ \text{J/kg}$ , the thermal conductivity of ice is  $k_i \approx 2.2\ \text{W/m}\cdot\text{K}$ , and  $\Delta T = T_w - 273\ \text{K} \sim 10\ \text{K}$ . It follows that  $v_f \sim 10^3\ \mu\text{m/s}$ , which means that a  $10\ \mu\text{m}$  droplet freezes in the order of 10 ms. This is negligible in comparison to the time taken to grow the inter-droplet ice bridge,  $\mathcal{O}(1\ \text{s})$ , that is required to initiate the intra-droplet freezing. Thus, the time taken for ice to percolate through one unit cell, comprising a step of average bridge length  $\langle L_b \rangle$  and jump of average droplet size  $\langle D_i \rangle$ , is given by  $t_p = (\langle L_b \rangle + \langle D_i \rangle) / v_p \approx \langle L_b \rangle / \langle v_b \rangle$ . Therefore,

$$\frac{v_p}{\langle v_b \rangle} \approx 1 + \frac{\langle D_i \rangle}{\langle L_b \rangle} \geq 1 + \frac{1}{\langle S^* \rangle}. \quad (3)$$

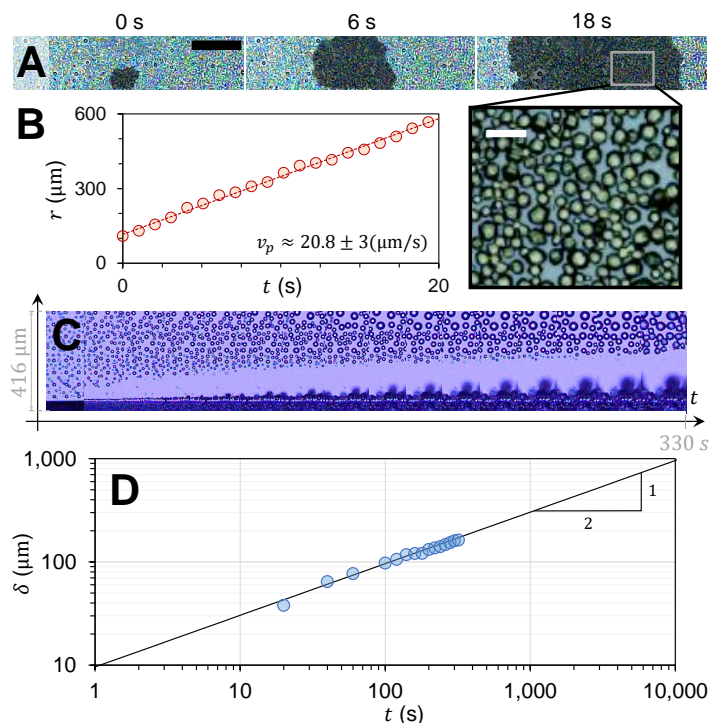


**Fig. 6** (A) Condensation frosting on a regular smooth hydrophobic surface at  $T_w = -25^\circ\text{C}$ ,  $T_\infty = 24^\circ\text{C}$  and  $RH = 65.2\%$ . The frozen droplets are false-colored black. The black and white scale bars denote  $200\ \mu\text{m}$  and  $50\ \mu\text{m}$ , respectively. (B) The tracking of the global front reveals a constant speed. (C) Time-lapse of a global failure of ice bridge connections, at  $T_w = -10^\circ\text{C}$ ,  $T_\infty = 23.5^\circ\text{C}$  and  $RH = 32\%$ . (D) Dry zone length plotted against time. The solid line follows  $\delta = 4.5 \sqrt{\mathcal{D}\Delta c/\rho} t^{1/2}$ .

The inequality at the end of Eq. 3 follows from the condition that  $L_b \leq L_{\max}$  for all local bridges to succeed, although  $\langle L_b \rangle$  and  $\langle D_l \rangle$  are global quantities. In order to test Eq. 3, we induced condensation frosting in an array of six  $\langle D_l \rangle \approx 30 \pm 2\ \mu\text{m}$  droplets on our chemical micropatterns with average separation  $\langle S^* \rangle = 1.06$ , by forming inter-droplet ice bridges of typical length  $\langle L_b \rangle \approx 10\ \mu\text{m}$  (Fig. 5A). The  $x-t$  plot of the freeze front in Fig. 5B captures both the steps corresponding to bridge growth rates,  $\langle v_b \rangle = 1.06 \pm 0.1\ \mu\text{m/s}$ , and the jumps corresponding to freezing the liquid droplets. Eq. 3 predicts that  $v_p/\langle v_b \rangle \approx 4$ . Indeed the experimentally measured percolation velocity was found to be  $v_p = 3.8\ \mu\text{m/s}$  (Fig. 5B, inset). Note that  $\langle D_l \rangle/\langle L_b \rangle$  in a sense physically represents how dense the droplets are packed.

Fig. 5C shows a 1D percolation front in a denser population ( $\langle S^* \rangle = 0.61$ ), where 31 successive droplets were frozen one after the other, until it was cut off at  $t = 31\ \text{s}$  when a frozen droplet from the left column grew an ice bridge to freeze the next droplet in the middle array. We track this 1D propagation in this middle row at 1 frame per second and plot it in (B). The resulting  $x-t$  plot (Fig. 5D) shows that there is a constant percolation velocity of  $v_p \approx 21.8\ \mu\text{m/s}$  (best-fit). The typical values of  $D_l = 21 \pm 1\ \mu\text{m}$  and  $v_b = 1.3\ \mu\text{m/s}$  (as obtained in Fig. 4), when plugged into Eq. 3 along with the best-fit of  $v_p$ , yields  $L_b \approx 1.33\ \mu\text{m}$ . This is consistent with experimentally observed values of  $L_b \leq 2\ \mu\text{m}$ , especially when considering that these measurements are approaching the spatial resolution of our images.

Finally we take the very general case of microcondensate grown on a regular smooth hydrophobic surface without any chemical micropatterning. The surface was cooled to  $T_w = -25^\circ\text{C}$ , with ambient conditions of  $T_\infty = 24^\circ\text{C}$  and  $65.2\%$  relative humidity. The high degree of supersaturation ( $S = 20.1$ ) resulted in a dense population of supercooled condensate. The series of micrographs in Fig. 6A shows an inter-droplet frost front, invading the field-of-view in the initial frame and radially spreading over the surface (false-colored black, see Fig. S4 in the Supplemental Material for original figure). The condensate had a typical size of  $D_l \sim 10\ \mu\text{m}$  ( $13 \pm 4\ \mu\text{m}$ ) over this particular time period. The inset zooms in to better depict individual frozen droplets and ice bridges. Four random points were chosen along the freeze front at the initial frame corresponding to  $t = 0$ , and were tracked over time to obtain  $r-t$  plots. The percolation speed was measured to be a constant  $v_p = 20.8 \pm 3\ \mu\text{m/s}$  over a time span of  $22.4\ \text{s}$  (Fig 6B), where the uncertainty represents a standard deviation over the four different speeds. This shows that coarse-grained percolation speeds appear constant when the time scale is of the order of  $10\ \text{s}$ . When looking at higher temporal resolutions of  $0.1 - 1\ \text{s}$ , the speed jumps between  $v_b$  and  $v_f$ , as seen in Fig. 5B in the manuscript. This finding shows how denser packings can lead to percolation speeds of  $\mathcal{O}(10\ \mu\text{m/s})$  both on micropatterned as well as smooth hydrophobic surfaces. Furthermore, our model of percolation speed, initially used with ordered droplets on the chemically patterned surface, also applies to arbitrarily nucleated condensate populations on smooth hydrophobic surfaces (as long as they are dense and fairly monodisperse).

$S^* > S_{Cr}^*$  everywhere: This case corresponds to a freezing event followed by a global failure of ice bridge connections due to the neighboring droplets completely evaporating (Fig. 6C). A global evaporation front develops, grows to a distance of  $\delta_{Cr} \sim 0.1 - 1\ \text{mm}$ , and comes to rest. Interestingly, while individual liquid droplets and isolated ice bridges evaporate and grow at a fairly constant rates, the evaporation front grows as  $\delta \sim t^{1/2}$  (Fig. 6D). This law can be rationalized by approximating the sea of droplets to be a thin liquid film of height  $h$ , where  $h \approx \langle D_l \rangle$ . This allows one to write the mass flux equation per unit width for the front as  $\rho h (d\delta/dt) \sim \mathcal{D}(\Delta c/\delta)h$ , resulting in:

$$\delta \sim \sqrt{\frac{\mathcal{D}\Delta c}{\rho}} t^{1/2}. \quad (4)$$

Eq. 4 accurately captures the experimental data in Fig. 6D (solid line) with a pre-factor of 4.5. This dynamical law reveals that in the early stages of dry zone formation, when  $\delta$  is on the order of a few droplet lengths, the evaporation front would grow as  $t^{1/2}$ . Such a balance is possible only when  $\delta$  is small enough that the evaporation flux, which goes as  $1/\delta$ , dominates over the condensation flux from the ambient ( $c_\infty U$ , where  $U$  is the velocity of vapor toward the substrate). As  $\delta$  increases, the evaporative flux becomes weaker and eventually becomes equal and opposite to the condensation flux. This critical distance  $\delta_{Cr} \sim \mathcal{D}\Delta c/(c_\infty U)$  is typically a few millimeters for our system.<sup>15,16,24</sup> This would imply that the  $\delta-t$  plot would eventually deviate from the  $1/2$ -law and come to an equilibrium. However, in our experiments, the

condensate is frozen by the invasion of ice bridges before this deviation could occur (last frame of the chronophotography image in Fig. 6C). Once the water droplets freeze, there is no in-plane source-sink interaction, such that the dry zone ceases to evolve any further.

In summary, we have shown that while the kinetics of inter-droplet ice bridging depend on surface temperature, wettability, and ambient conditions, the criterion for connecting a bridge to a liquid droplet is surprisingly independent of all of these parameters. From extensive experiments with droplet sizes ranging from  $1\ \mu\text{m}$ – $10\ \text{mm}$ , the success or failure of an ice bridge was only a function of the droplet size, inter-droplet distance, and the ratio comparing the sizes of the liquid and frozen droplets. The growth rate of an individual ice bridge was found to be constant for fairly monodisperse populations of microcondensate, which we explained using an electrostatic analogy. When simplifying to the two limiting cases of all bridges connecting or failing, the spread of global percolation fronts scaled with  $t^1$  or  $t^{1/2}$  behaviors, respectively. These laws hold as long as the bridge lengths are short,  $L_b \lesssim \lambda$ , where  $\lambda \sim 10\ \mu\text{m}$ . When  $L_b$  is  $100\ \mu\text{m}$  or larger, the resulting instabilities of the desublimating front greatly affect the dynamics of condensation frosting in a manner that remains to be studied. Whether ice bridges the gap or not, we hope this article will bridge the gap between surface scientists and cloud physicists with a shared appreciation of the importance of source-sink interactions in mixed-phase droplet populations.

## Conflicts of interest

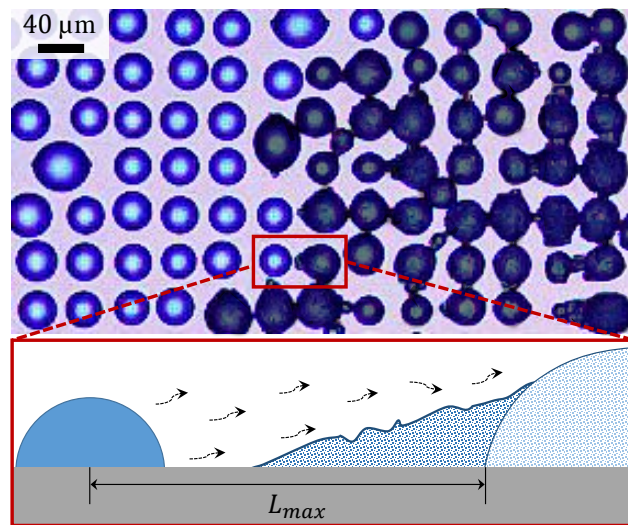
There are no conflicts to declare.

## Acknowledgements

This work was supported by the National Science Foundation (CBET-1604272). S.N. thanks Daniel Beysens and David Quéré for a critical reading of the manuscript and fruitful discussions. S. N. acknowledges the support of the European Union's Horizon 2020 research and innovation program LubISS (Marie Skłodowska-Curie grant agreement No 722497).

## Notes and references

- 1 A. Wegener, *Thermodynamik der Atmosphäre*, Leipzig, 1911, p. 331.
- 2 T. Bergeron, *Int. Union of Geodesy and Geophysics, Paris, France*, 1935, **156**, year.
- 3 W. Findeisen, *Meteor. Z.*, 1938, **55**, 121–133.
- 4 A. V. Korolev and I. P. Mazin, *J. Atmos. Sci.*, 2003, **60**, 2957–2974.
- 5 J. B. Dooley, *PhD thesis*, Texas A & M, 2010.
- 6 J. B. Boreyko and C. P. Collier, *ACS Nano*, 2013, **7**, 1618–1627.
- 7 J. Guadarrama-Cetina, A. Mongruel, W. Gonzalez-Vinas and D. Beysens, *Europhys. Lett.*, 2013, **101**, 16009.
- 8 S. Nath, S. F. Ahmadi and J. B. Boreyko, *Nanosc. Microsc. Therm.*, 2017, **21**, 81–101.
- 9 S. Jung, M. K. Tiwari and D. Poulikakos, *Proc. Natl. Acad. Sci. U.S.A.*, 2012, **109**, 16073–16078.
- 10 X. Chen, R. Ma, H. Zhou, X. Zhou, L. Che, S. Yao and Z. Wang, *Sci. Rep.*, 2013, **3**, 2515.
- 11 S. Chavan, D. Park, N. Singla, P. Sokalski, K. Boyina and N. Miljkovic, *Langmuir*, 2018, **34**, 6636–6644.
- 12 R. Bohm, M. R. Haque, C. Qu, E. C. Kinzel and A. R. Betz, *AIP Adv.*, 2018, **8**, 125228.
- 13 J. B. Boreyko, R. R. Hansen, K. R. Murphy, S. Nath, S. T. Retterer and C. P. Collier, *Sci. Rep.*, 2016, **6**, 19131.
- 14 S. Nath and J. B. Boreyko, *Langmuir*, 2016, **32**, 8350–8365.
- 15 S. Nath, C. E. Bisbano, P. Yue and J. B. Boreyko, *J. Fluid Mech.*, 2018, **853**, 601–620.
- 16 J. Guadarrama-Cetina, A. Mongruel, W. Gonzalez-Vinas and D. Beysens, *Europhys. Lett.*, 2015, **110**, 56002.
- 17 S. F. Ahmadi, S. Nath, G. J. Iloff, B. R. Srijanto, C. P. Collier, P. Yue and J. B. Boreyko, *ACS Appl. Mater. Interfaces*, 2018, **10**, 32874–32884.
- 18 J. S. Langer, *Reviews of Modern Physics*, 1980, **52**, 1.
- 19 A. J. D. Shaikeea and S. Basu, *Langmuir*, 2016, **32**, 1309–1318.
- 20 D. M. Murphy and T. Koop, *Q. J. R. Meteorol. Soc.*, 2005, **131**, 1539–1565.
- 21 H. R. Pruppacher, J. D. Klett and K. P. Wang, *Microphysics of Clouds and Precipitation*, Taylor & Francis, 1998.
- 22 J. B. Boreyko and C. H. Chen, *Phys. Rev. Lett.*, 2009, **103**, 184501.
- 23 J. Petit and E. Bonaccorso, *Langmuir*, 2014, **30**, 1160–1168.
- 24 J. Guadarrama-Cetina, R. D. Narhe, D. A. Beysens and W. Gonzalez-Vinas, *Phys. Rev. E*, 2014, **89**, 012402.



We develop models to rationalize the growth of inter-droplet ice bridges that govern condensation frosting on chilled surfaces.